





Article

# Surface Modification of FeCoNiCr Medium-Entropy Alloy (MEA) Using Octadecyltrichlorosilane and Atmospheric-Pressure Plasma Jet

Pei-Yu Cheng <sup>1,2</sup>, Nian-Hu Lu <sup>3</sup>, Yi-Sheng Lu <sup>4</sup>, Chih-Hsuan Chen <sup>3,\*</sup>, Yueh-Lien Lee <sup>4,\*</sup> and Jian-Zhang Chen <sup>1,2,\*</sup>

<sup>1</sup> Graduate Institute of Applied Mechanics, National Taiwan University, Taipei City 10617, Taiwan; r07543033@ntu.edu.tw

<sup>2</sup> Advanced Research Center for Green Materials Science and Technology, National Taiwan University, Taipei City 10617, Taiwan

<sup>3</sup> Department of Mechanical Engineering, National Taiwan University, Taipei City 10617, Taiwan; f06522712@ntu.edu.tw

<sup>4</sup> Department of Engineering Science and Ocean Engineering, National Taiwan University, Taipei City 10617, Taiwan; r06525019@ntu.edu.tw

\* Correspondence: chchen23@ntu.edu.tw (C.-H.C.); yuehlien@ntu.edu.tw (Y.-L.L.); jchen@ntu.edu.tw (J.-Z.C.); Tel.: +886-2-33665694 (J.-Z.C.)

Received: 15 March 2020; Accepted: 30 March 2020; Published: 2 April 2020



**Abstract:** Surface condition and corrosion resistance are major concerns when metallic materials are going to be utilized for applications. In this study, FeCoNiCr medium-entropy alloy (MEA) is first treated with a nitrogen atmospheric-pressure plasma jet (APPJ) and then coated with octadecyltrichlorosilane (OTS) for the surface modification. The hydrophobicity of the FeCoNiCr MEA was effectively improved by OTS-coating treatment, APPJ treatment, or the combination of both treatments (OTS-coated APPJ-treated), which increased the water contact angle from 54.49° of the bare MEA to 70.56°, 93.94°, and 88.42°, respectively. Potentiodynamic polarization and electrochemical impedance spectroscopy tests demonstrate that the APPJ-treated FeCoNiCr MEA exhibits the best anti-corrosion properties. X-ray photoelectron spectroscopy reveals that APPJ treatment at 700 °C oxidizes all the alloying elements in the FeCoNiCr MEA, which demonstrates that a short APPJ treatment of two-minute is effective in forming a metal oxide layer on the surface to improve the corrosion resistance of FeCoNiCr MEA. These results provide a convenient and rapid method for improving surface properties of FeCoNiCr MEA.

**Keywords:** atmospheric-pressure plasma jet; surface treatment; hydrophobicity; medium entropy alloy; oxidation; octadecyltrichlorosilane

## 1. Introduction

Medium-entropy alloys (MEAs) contain multiple principal elements with high mixing entropy for stabilization in a disordered solid solution state [1–4]. In particular, FeCoNiCrMn-based materials have attracted attention for their excellent combination of properties such as good fracture resistance, high tensile strength and ductility, excellent cryogenic properties, and superplasticity. This alloy family is based on face-centered cubic (fcc) FeCoNiCr solid solution [5]. Due to the high potential for applications, various methods were introduced to further improve the properties of FeCoNiCr MEA, including elemental alloying [6,7], precipitation hardening [8,9], and processing [10,11]. To utilize MEAs into real applications, their surface properties and corrosion resistance are critical concerns.

Because MEAs contain multiple principal elements, their oxidation and corrosion behaviors are usually quite complicated and have been investigated widely [4,12–14].

Octadecyltrichlorosilane (OTS) is a frequently used chemical for modifying the hydrophilic –OH attached surface into a hydrophobic surface [15–17]. By well controlling the immersion time, water content, and silane concentration, a self-assembled monolayer (SAM) could be formed on the oxide surface [18–20]. The quality of the oxide underneath also influences the quality of the grown SAM [18]. A silane coating has been used for improving the anticorrosion properties of metals and alloys [21,22]. Typically, MEAs have native oxides on the surface, and therefore, it is possible to modify the surface of a MEA with silane-based molecules. Because the quality of the oxide underneath could influence the quality of the follow-up deposited SAM, an atmospheric-pressure plasma jet (APPJ) is employed to oxidize FeCoNiCr MEAs prior to OTS coating.

An atmospheric-pressure plasma (APP) can be operated at regular pressure without using vacuum systems that demand routine maintenance. Several techniques have been used to develop a stable APP, including transfer arc, corona, dielectric barrier discharge, and APPJ [23–27]. Various electrode configurations and excitation methods generate APPs with different gas and electron temperatures [28]. APP with low gas temperature has been used for applications in biomedicine, food processing, and agriculture [29,30]. An APP with an intermediate gas temperature (of the order of several hundred degrees Celsius) can be used for rapid materials processing by taking advantage of the synergetic effect of heat and reactive plasma species [28,31–41]. APP has been used to oxidize the AA6061-T6 aluminum alloy surface for strong and durable adhesive bonding applications [42]. An APPJ has also been used for generating a corrosion protection for a copper surface [43]. An APP polymerized fluorine-rich coating demonstrated to enhance corrosion resistance and hemocompatibility for a biomedical NiTi alloy [44].

In this study, we experimentally test a nitrogen APPJ with working temperature of ~700 °C to oxidize the surface of FeCoNiCr MEAs. Then, OTS is used to modify the surface. With these surface modification treatments, the hydrophobicity, corrosion resistance and surface bonding conditions of the FeCoNiCr MEA are investigated and analyzed to understand the improvement of surface properties.

## 2. Experimental Detail

### 2.1. Preparation of FeCoNiCr MEA

The equiatomic FeCoNiCr MEA was prepared by vacuum arc melting under a high-purity Ar atmosphere. High-purity (>99.9 wt %) Fe, Co, Ni, and Cr elements were used as raw materials. Before melting the FeCoNiCr ingot, a pure Ti ingot was melted two times to reduce the oxygen content in the chamber. To improve the chemical homogeneity of the material, the FeCoNiCr ingot was flipped and remelted six times. The ingot was homogenized at 1200 °C for 24 h under Ar atmosphere in a tubular furnace and then subjected to furnace cooling. The homogenized ingot was then cold-rolled to an 80% reduction in thickness. The cold-rolled plate was then annealed at 900 °C for 1 h and then cut into 2 × 2 cm samples using a diamond saw.

### 2.2. Pretreatment of FeCoNiCr MEA before APPJ Treatment

First, the FeCoNiCr MEA specimens were mechanically abraded using sand paper with mesh number up to P2000. Next, the specimens were sequentially ultrasonicated in deionized water, acetone, and isopropanol; each ultrasonication was performed for 15 min. After ultrasonication, the specimens were blow-dried using a N<sub>2</sub> gun.

### 2.3. APPJ Treatment of FeCoNiCr MEA

Figure 1a shows the APPJ setup used in this study. The voltage, frequency, and duty cycle of the APPJ were 275 V, 25 kHz, and 17.5%, respectively. The N<sub>2</sub> flow rate was fixed as 34 standard liters per minute (slm). Reduce the air-quenching effect from ambient air, a quartz tube with length of 4.5 cm and internal diameter of 3 cm was installed downstream of the plasma jet exit. This arrangement can

increase the plasma jet length and expand the plasma influential zone. The temperature at the sample surface was monitored using a K-type thermocouple. Figure 1b shows the temperature evolution. The temperature plateaued at  $\sim 700$  °C. The APPJ treatment lasted for 2 min. Figure 1c shows the photograph of APPJ during processing.

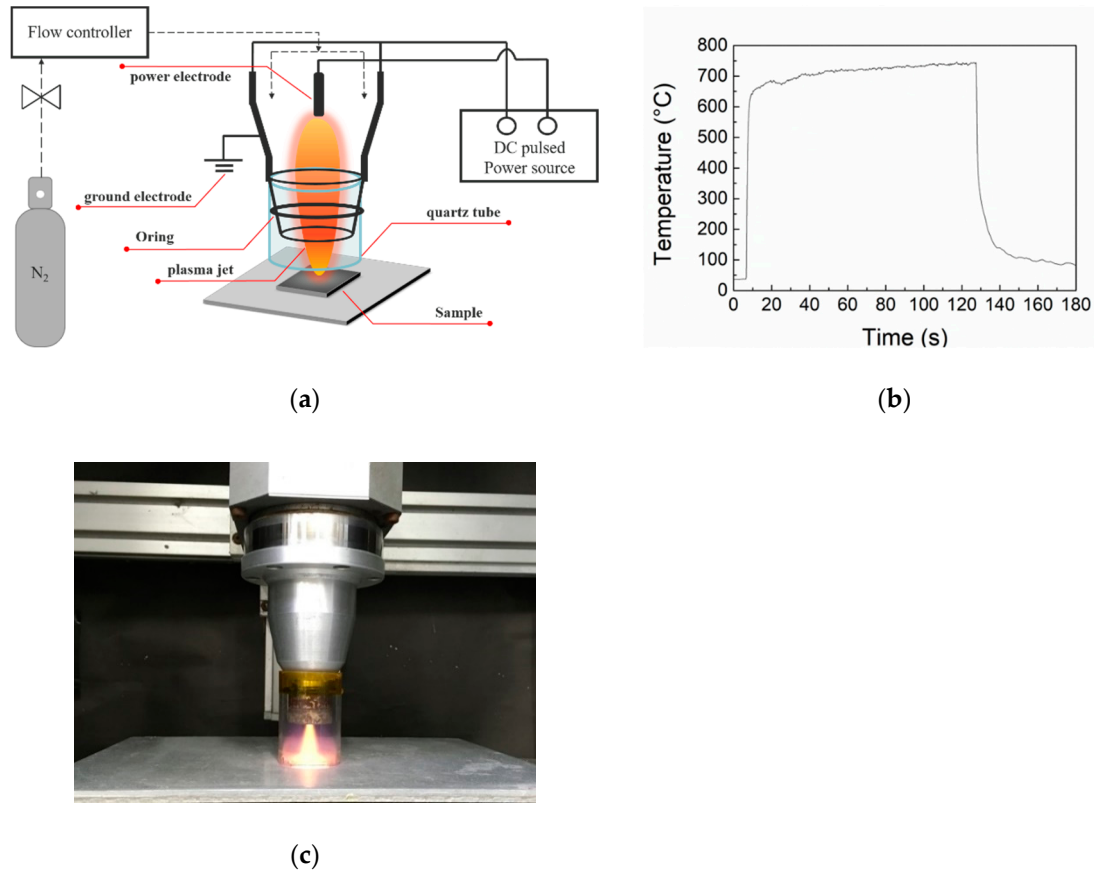


**Figure 1.** (a) Schematic of atmospheric-pressure plasma jet (APPJ) setup; (b) working temperature evolution of APPJ; (c) photograph of APPJ during processing.

#### 2.4. OTS Coating

The OTS coating is performed using a solution process. First, 4  $\mu$ L of OTS (95%, Acros Organics, Waltham, MA, USA) was injected into 10 mL of n-dodecane (99+%, Alfa Aesar, Ward Hill, MA, USA) in a beaker. FeCoNiCr MEA specimens with/without APPJ treatment were immersed in the solution with ultrasonication for 15 min. Figure 2 shows the OTS self-assembly reaction process. It is generally accepted that OTS molecules are either chemisorbed or physisorbed on the oxide surface with some molecules forming short-range cross-linked structures [15].

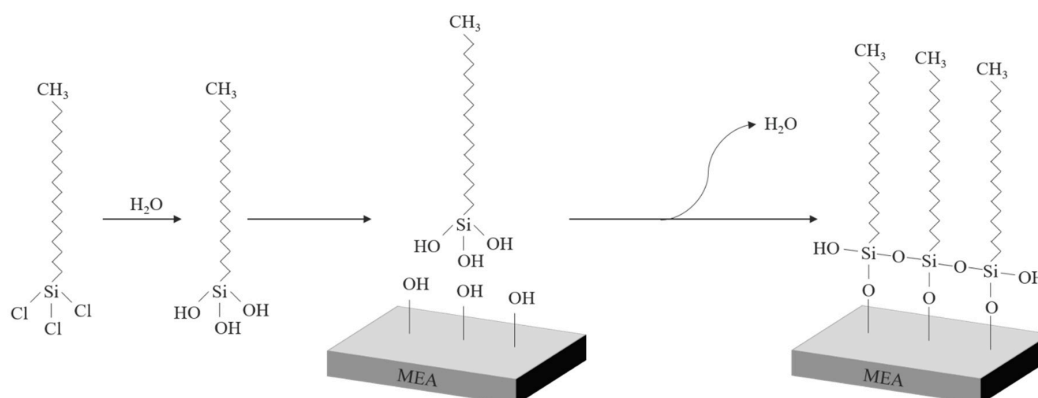


**Figure 2.** Schematic diagram of octadecyltrichlorosilane (OTS) self-assembly reaction process.

### 2.5. Materials Characterization

The water contact angle was measured using a goniometer (Model 100SB, Sindatek Instruments Co., Ltd., New Taipei City, Taiwan). An electrochemical workstation (Metrohm Autolab, PGSTAT204, Ionenstrasse, Switzerland) was used to evaluate the corrosion resistance behavior of specimens in a 3.5 wt % NaCl through potentiodynamic polarization tests and electrochemical impedance spectroscopy (EIS) tests. A standard three-electrode system was used for electrochemical measurements. The specimen is the working electrode, a platinum wire and Ag-AgCl is used as the counter and reference electrodes, respectively. The potentiodynamic polarization test is performed starting from a potential from  $-0.5$  to  $1$  mV v.s. open circuit potential (OCP) at a scan rate of  $1$  mV/s. The EIS plots were acquired at OCP in a frequency range of  $10^5$ – $10^{-2}$  Hz by using an alternating current with the amplitude of  $10$  mV (rms). The surface chemical bonding status was investigated using X-ray photoelectron spectrometry (XPS, VGS Thermo Scientific K-Alpha, Waltham, MA, USA). The binding energy (BE) was calibrated with a C1s peak at  $284.8$  eV. The crystallinity was inspected using an X-ray diffractometer (XRD, Bruker D8 DISCOVER SSS Multi-Function High-Power X-Ray Diffractometer, Billerica, MA, USA). The surface morphology was inspected using a scanning electron microscope (SEM, JOEL JSM-7800 Prime, Tokyo, Japan).

### 3. Results and Discussion

Figure 3a shows the water contact angle ( $59.49^\circ$ ) for FeCoNiCr MEA without OTS and APPJ processing. After APPJ processing, the water contact angle increased to  $70.56^\circ$ , as shown in Figure 3b, possibly owing to the oxidation of FeCoNiCr MEA. Figure 3c shows the water contact angle after APPJ and OTS processing. The water contact angle is  $93.94^\circ$ . For comparison, we also performed OTS-coating on FeCoNiCr MEA without APPJ treatment; the water contact angle is  $88.42^\circ$ , as shown in Figure 3d. OTS coating significantly increased the water contact angle and hydrophobicity, indicating successful coating of OTS on FeCoNiCr MEA. With APPJ processing followed by OTS coating, the water contact angle is the largest, possibly owing to the formation of surface oxides that could facilitate the follow-up OTS coating. With a better quality of the OTS coating layer, the hydrophobicity of the FeCoNiCr surface is further improved.



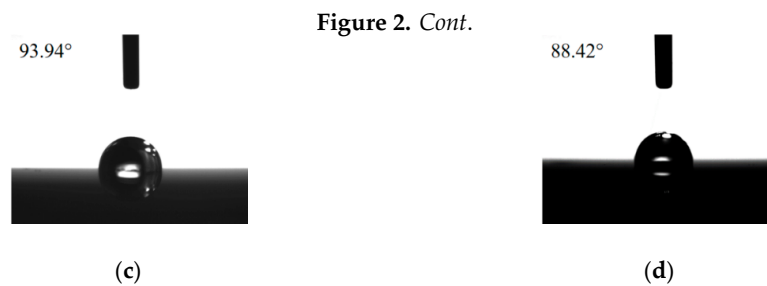


**Figure 3.** Water contact angles of (a) FeCoNiCr medium-entropy alloy (MEA), (b) APPJ-treated FeCoNiCr MEA, (c) OTS-coated APPJ-treated FeCoNiCr MEA, and (d) OTS-coated FeCoNiCr MEA.

Figure 4 shows the potentiodynamic polarization curves. FeCoNiCr, FeCoNiCr\_OTs, FeCoNiCr\_APPJ, and FeCoNiCr\_APPJ\_OTs represent bare, OTS-coated, APPJ-treated, and OTS-coated APPJ-treated FeCoNiCr MEAs, respectively. Table 1 lists the corresponding corrosion potential ( $E_{corr}$ ), corrosion current density ( $I_{corr}$ ), pitting potential ( $E_{pit}$ ), and passive region ( $E_{pit}-E_{corr}$ ) values determined with methods described in [45,46]. As shown from the table, APPJ treatment can increase pitting potential and passive region range of FeCoNiCr MEA. In addition, APPJ treatment also reduces the current density in the passive region. This enhancement in anti-corrosion properties can be attributed to the formation of metal oxides on the surface of FeCoNiCr MEA. However, the lower pitting potential and narrower passive region were observed in OTS-coated APPJ-treated FeCoNiCr MEA sample. It is plausible that the ultrasonication during OTS coating may produce defects on part of the loosely grown oxides during APPJ treatment. Nevertheless, APPJ treatment increases  $E_{corr}$  from  $-0.045$  V to  $0.006$  V. OTS coating does not drastically affect the corrosion potential and the current density in the passivation area compared with the bare and APPJ-treated MEAs. The OTS coating treatment after APPJ treatment improves the  $E_{corr}$  further to  $0.022$  V, however, the passive region drops to a level worse than the one without any treatment. Following the analyses, although the OTS coating increases the water contact angle, as shown in Figure 3, it seems not to be a suitable protective layer to prevent corrosion. In the end, the APPJ-treated MEA shows the best anti-corrosion performance based on the indicators of the pitting potential and the width of the passive region range. Figure S1 shows the XRD results, and Table S1 summarized corresponding crystallinity information obtained from XRD results in Figure S1. After the APPJ treatment, the grain size slightly increased because of the thermal effect. The relation between crystal size and corrosion may vary among different materials. In one particular case, the previous report indicates that grain size of 304L austenitic stainless steel has no effect on pitting potential [45].

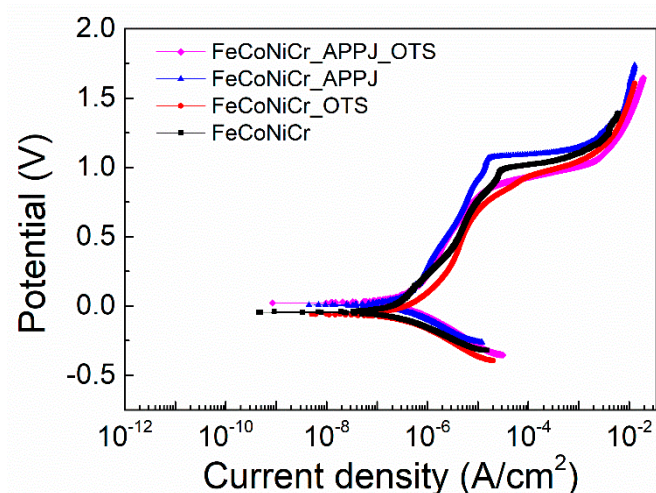


**Figure 4.** Potentiodynamic polarization test curves of bare, OTS-coated, APPJ-treated, and OTS-coated APPJ-treated FeCoNiCr MEAs.

**Table 1.**  $E_{corr}$  and  $I_{corr}$  for bare, OTS-coated, APPJ-treated, and OTS-coated APPJ-treated FeCoNiCr MEAs. Three measurements were performed.

Sample	$E_{corr}$ (V)	$I_{corr}$ ( $\mu\text{A}/\text{cm}^2$ )	$E_{pit}$ (V)	$\Delta E = E_{pit} - E_{corr}$ (V)
FeCoNiCr	$-0.069 \pm 0.013$	$53.2 \pm 32.3$	$0.997 \pm 0.020$	1.066
FeCoNiCr_APPJ	$-0.046 \pm 0.029$	$60.5 \pm 31.9$	$1.068 \pm 0.005$	1.114
FeCoNiCr_OTs	$-0.064 \pm 0.018$	$51.2 \pm 11.3$	$0.772 \pm 0.011$	0.836
FeCoNiCr_APPJ_OTs	$-0.021 \pm 0.022$	$54.5 \pm 0.8$	$0.826 \pm 0.004$	0.847

From potentiodynamic polarization curves, APPJ treated-MEA shows better corrosion-resistant properties. For clarity, hereafter we compare data with bare MEA and APPJ-treated MEA. Figure 5 shows the results of the EIS plots of bare and APPJ-treated MEAs. Figure 5a,b show the comparative results of Bode magnitude and Bode phase plots from two types of samples after first hour of immersion. The evolution of EIS Bode plots from two types of samples during immersion time up to 12 h is reported in Figure 5c,d. The EIS measurement results for all cases (bare, APPJ-treated, OTS-coated, OTS-coated APPJ-treated MEAs) are listed in the Supplementary Information.

As can be seen in Figure 5a,b, the impedance value at low frequency ( $|Z|_{0.01\text{Hz}}$ ) of APPJ-treated MEA ( $112995\Omega$ ) was higher than that of bare MEA ( $50704\Omega$ ) at the beginning of the EIS measurement. Although a slight decrease of  $|Z|_{0.01\text{Hz}}$  for APPJ-treated FeCoNiCr MEA was observed as the immersion time increased, as shown in Figure 5d, APPJ-treated FeCoNiCr MEA still exhibited a higher  $|Z|_{0.01\text{Hz}}$  value compared with that obtained from bare FeCoNiCr MEA, suggesting that APPJ treatment can enhance the anti-corrosion properties of FeCoNiCr MEA. In addition, Figures S2–S5 show the details of EIS plots for each specimen.

Figure 6 shows the XPS survey scan spectra of FeCoNiCr and APPJ-treated FeCoNiCr MEAs. Table 2 lists the atomic contents analyzed from Figure 6. Carbon content decreased [43] and oxygen content increased after APPJ processing, indicating the removal of organic contaminants and oxidation of FeCoNiCr MEA.

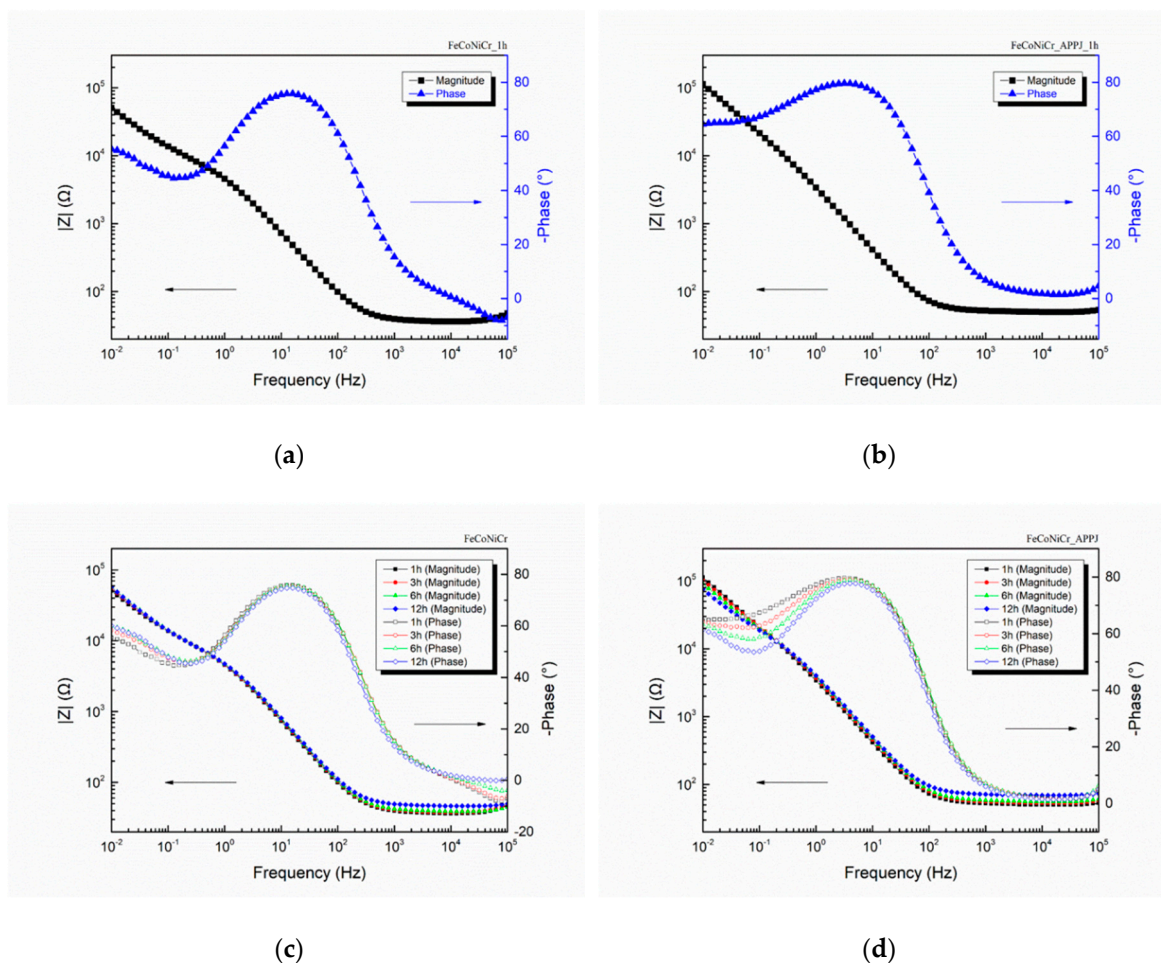


**Figure 5.** Bode magnitude and Bode phase plots of (a) bare MEA after 1 h, (b) APPJ-treated MEA after 1 h, (c) bare MEA for 12 h, and (d) APPJ-treated MEA for 12 h.

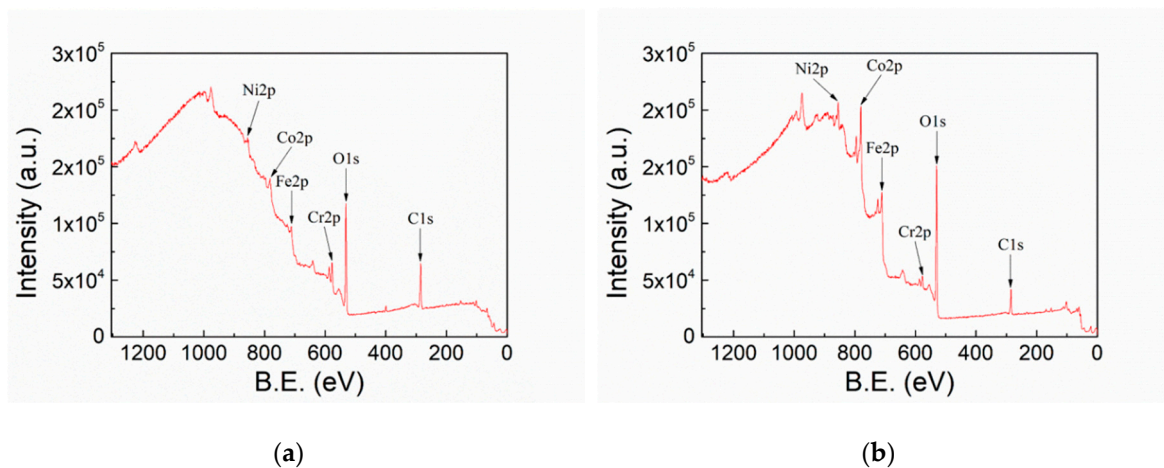


**Figure 6.** XPS survey scan spectra of (a) FeCoNiCr and (b) APPJ-treated FeCoNiCr.

**Table 2.** Elemental ratios from XPS survey scan in Figure 6.

	C1s (at%)	O1s (at%)	N1s (at%)	Cr2p (at%)	Fe2p (at%)	Ni2p (at%)	Co2p (at%)
FeCoNiCr	42.25%	39.68%	4.62%	4.79%	2.94%	2.59%	3.12%
FeCoNiCr_APPJ	16.1%	49.9%	1.47%	2.41%	13.09%	4.21%	12.81%

Figure 7 shows the XPS O1s spectra of FeCoNiCr and APPJ-treated FeCoNiCr MEAs. Deconvoluted peaks represent  $O_{2+}$  (530 eV), OH (531.6 eV), and  $H_2O$  (532.8 eV) [4]. Table 3 lists the areal atomic ratio of these contents. After APPJ treatment, the overall peak intensity significantly increased, suggesting the occurrence of oxidation. Figure 8 shows the XPS Fe2p spectra that can be deconvoluted into four components, metallic Fe (706.6 eV),  $Fe_{ox}^{2+}$  (708.2 eV),  $Fe_{ox}^{3+}$  (709.8 eV), and  $Fe_{hy}^{3+}$  (711.6 eV) [4,46]. Table 4 lists the ratio of these four components. Metallic Fe ( $Fe^0$ ) content significantly decreased from 15.10% to 0% and  $Fe^{2+}$  decreased from 3.4% to 0%, whereas  $Fe^{3+}$  increased from 19.06% to 49.23%; this strongly suggests the oxidation of the Fe component by APPJ treatment. Fe is oxidized into  $Fe^{3+}$  state after APPJ processing. Figure 9 shows the XPS Co2p spectra and Table 5 lists the ratio of deconvoluted components, metallic Co (777.5 eV),  $Co_3O_4$  (779.8 eV), CoO (780.3 eV),  $Co(OH)_2$  (781.2 eV),  $Co_2O_3$  (780.4 eV), and  $Co_2N_3$  (778.1 eV) [4,47,48]. No metallic Co was detected even without APPJ treatment, implying high oxidization proportion of Co on the surface. After APPJ treatment, alteration of cobalt oxide status was noted. The whole surface was in the oxidized state for Co. No Co nitridation was noted with nitrogen APPJ treatment. Figure 10 shows the XPS Ni2p spectra that can be deconvoluted into Ni (852.4 eV), NiO (853.8 eV),  $Ni(OH)_2$  (856.7 eV),  $Ni_2O_3$  (855.3 eV),  $NiO_{sat.}$  (860.8 eV),  $Ni(OH)_2_{sat.}$  (862.3 eV), and  $Ni_2O_3_{sat.}$  (861.2 eV) [4,49]. Table 6 lists the component ratio. After APPJ processing, all Ni components including large portions of metallic Ni and NiO and a small amount of  $Ni(OH)_2$  were oxidized into  $Ni_2O_3$ . Before APPJ treatment, the surface of FeCoNiCr MEA contained 16.59% metallic Ni and 44.36% NiO. All these components were completely oxidized into  $Ni_2O_3$ . Figure 11 shows the XPS Cr2p spectra that can be deconvoluted into metallic Cr (574 eV),  $Cr_2O_3$  (576.3 eV), and  $Cr(OH)_3$  (577.1 eV) [4,50,51]. Table 7 lists the ratio of each component. Before APPJ treatment, 13.22% metallic Cr was seen on the surface. After APPJ treatment, the metallic Cr content reduced to 0% and the  $Cr(OH)_3$  component increased. This also indicates oxidation of Cr by APPJ processing. Overall, all metal components in FeCoNiCr MEA were oxidized by nitrogen APPJ treatment because of the involvement of oxygen from ambient air in APPJ processing. The APPJ temperature was set as 700 °C; in this high-temperature environment, MEA oxidation occurred easily. The oxidations of all the metallic components in the FeCoNiCr MEA formed effective surface oxide layer which contributed to the better follow-up OTS treatment and the better corrosion resistance. Experimental results demonstrate that APPJ treatment is a convenient and economic method to improve the anti-corrosion properties of FeCoNiCr MEA. Furthermore, Figure S6 shows the SEM images of specimens of bare, APPJ-treated, OTS-coated APPJ-treated and OTS-coated MEAs. No apparent morphology difference is noted.

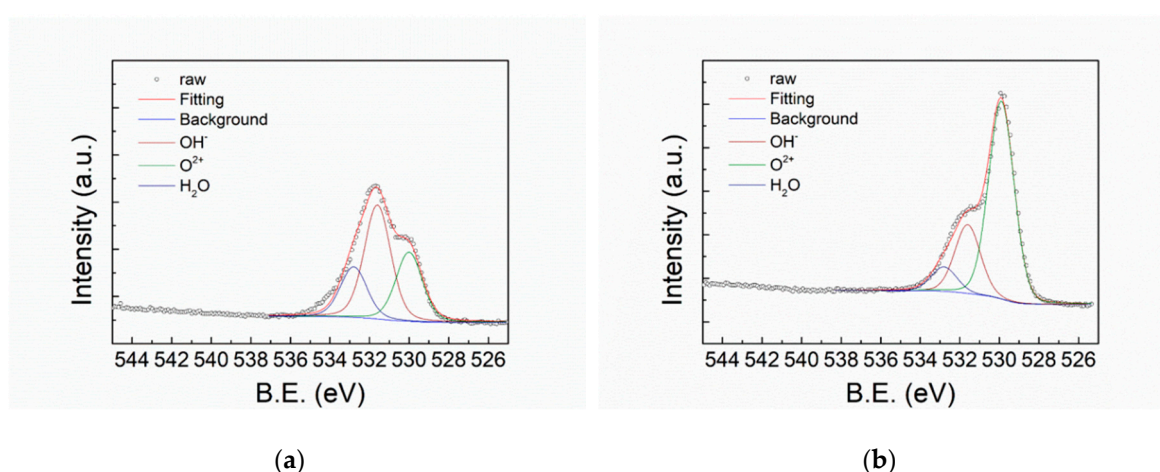
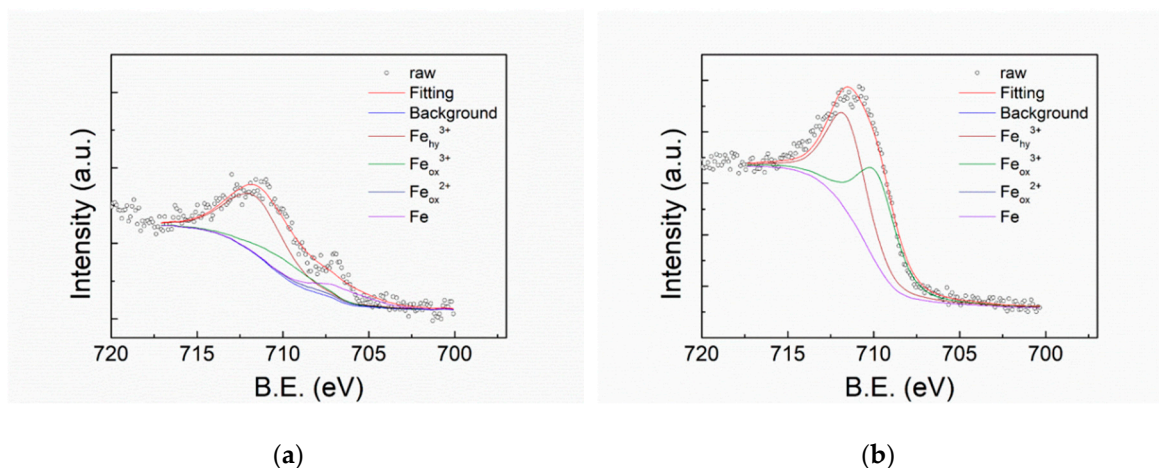


Figure 7. XPS O1s spectra of (a) FeCoNiCr and (b) APPJ-treated FeCoNiCr MEAs.



**Table 3.** XPS O1s deconvoluted peak areal ratios from XPS spectra shown in Figure 7.

	O <sup>2+</sup> (at%)	OH <sup>-</sup> (at%)	H <sub>2</sub> O (at%)
FeCoNiCr	29.57%	48.84%	21.60%
FeCoNiCr_APPJ	67.97%	23.65%	8.38%



**Figure 8.** XPS Fe2p spectra of (a) FeCoNiCr and (b) APPJ-treated FeCoNiCr MEAs.

**Table 4.** XPS Fe2p deconvoluted peak areal ratios from XPS spectra shown in Figure 8.

	Fe (at%)	Fe <sub>ox</sub> <sup>2+</sup> (at%)	Fe <sub>ox</sub> <sup>3+</sup> (at%)	Fe <sub>hy</sub> <sup>3+</sup> (at%)
FeCoNiCr	15.10%	3.40%	19.06%	62.44%
FeCoNiCr_APPJ	0.00%	0.00%	49.23%	50.77% <sup>1</sup>

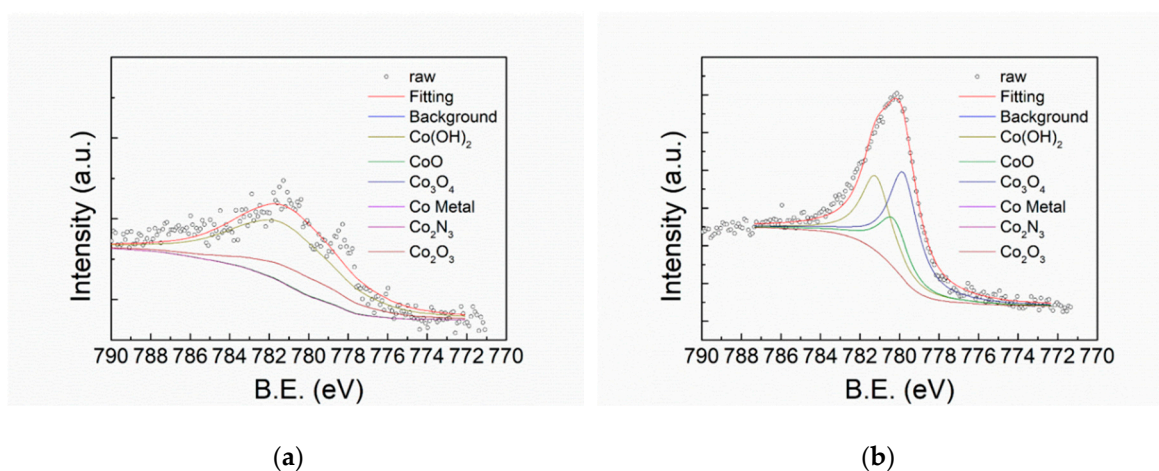


**Figure 9.** XPS Co2p spectra of (a) FeCoNiCr and (b) APPJ-treated FeCoNiCr MEAs.

**Table 5.** XPS Co2p deconvoluted peak areal ratios from XPS spectra shown in Figure 9.

	Co Metal (at%)	Co <sub>3</sub> O <sub>4</sub> (at%)	CoO (at%)	Co(OH) <sub>2</sub> (at%)	Co <sub>2</sub> O <sub>3</sub> (at%)	Co <sub>2</sub> N <sub>3</sub> (at%)
FeCoNiCr	0.00%	0.00%	0.67%	75.66%	23.67%	0.00%
FeCoNiCr_APPJ	0.00%	46.33%	21.25%	32.42%	0.00%	0.00%

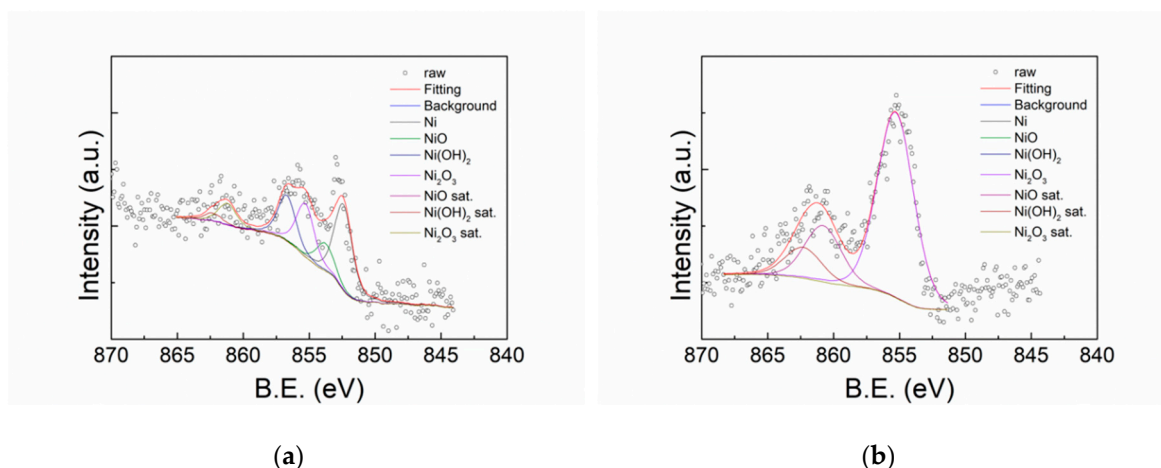


Figure 10. XPS Ni<sub>2p</sub> spectra of (a) FeCoNiCr and (b) APPJ-treated FeCoNiCr MEAs.

Table 6. XPS Ni<sub>2p</sub> deconvoluted peak areal ratios from XPS spectra shown in Figure 10.

	Ni (at%)	NiO (at%)	Ni(OH) <sub>2</sub> (at%)	Ni <sub>2</sub> O <sub>3</sub> (at%)
FeCoNiCr	16.59%	44.36%	0.20%	38.85%
FeCoNiCr_APPJ	0.00%	0.00%	0.00%	100.00%

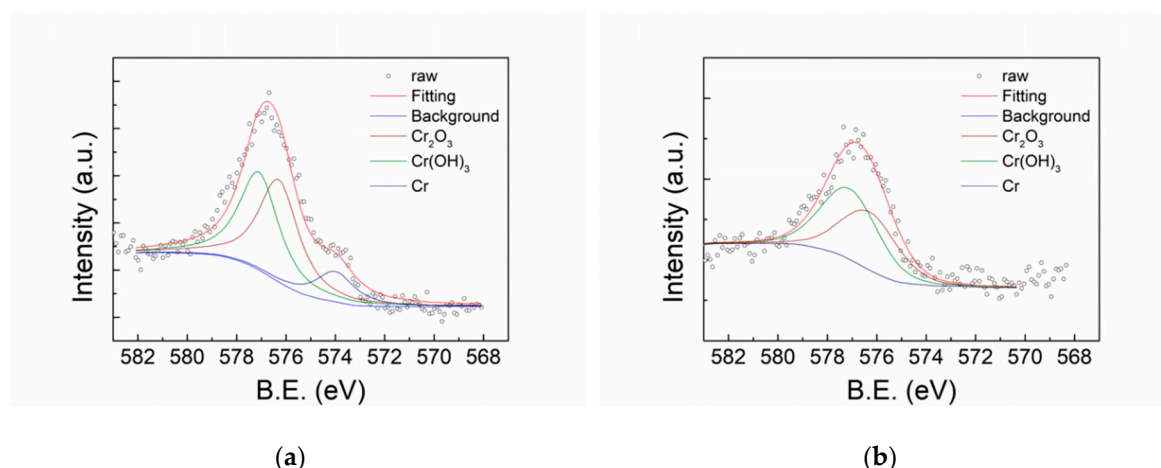


Figure 11. XPS Cr<sub>2p</sub> spectra of (a) FeCoNiCr and (b) APPJ-treated FeCoNiCr MEAs.

Table 7. XPS Cr<sub>2p</sub> deconvoluted peak areal ratios from XPS spectra shown in Figure 11.

	Cr (at%)	Cr <sub>2</sub> O <sub>3</sub> (at%)	Cr(OH) <sub>3</sub> (at%)
FeCoNiCr	13.22%	44.47%	42.32%
FeCoNiCr_APPJ	0.00%	45.13%	54.87%

#### 4. Summary

We use a nitrogen APPJ and OTS coating for the surface modification of FeCoNiCr MEA. A short nitrogen APPJ treatment for 2 min at 700 °C oxidized FeCoNiCr MEA. The metal oxide layer resulted from the APPJ treatment not only increases the passivation region and pitting potential but also decreases the current density of the passivation area. An OTS coating improves the hydrophobicity but narrows down the passivation region. Nevertheless, an OTS coating does not drastically influence the corrosion potential, the corrosion rate, and the current density in the passivation area. OTS-coated APPJ-treated FeCoNiCr MEA shows the highest hydrophobicity with water contact angle of 93.94°.

however, APPJ-treated FeCoNiCr MEA shows the best anti-corrosion property. The APPJ and OTS coating methods introduced in this study provide convenient and economic surface modifications to improve the corrosion resistance and surface hydrophobicity of FeCoNiCr MEA.

**Supplementary Materials:** The following are available online at <http://www.mdpi.com/2073-4360/12/4/788/s1>, Figure S1: Low-angle X-ray diffraction (XRD) of the FeCoNiCr alloy, Table S1: The crystallinity properties obtained from Figure S1, Figure S2: (a) Magnitude diagram and (b) phase diagram of the Bode plots, and (c) the Nyquist plots with EIS measurement of bare MEA for 12 h, Figure S3: (a) Magnitude diagram and (b) phase diagram of the Bode plots, and (c) the Nyquist plots with 12-h EIS measurement of APPJ-treated MEA for 12 h, Figure S4: (a) Magnitude diagram and (b) phase diagram of the Bode plots, and (c) the Nyquist plots with 12-h EIS measurement of OTS-coated MEA, Figure S5: (a) Magnitude diagram and (b) phase diagram of the Bode plots, and (c) the Nyquist plots with 12-h EIS measurement of OTS-coated APPJ-treated MEA. Figure S6: SEM images (magnification rate =5000X) of (a) bare, (b) APPJ-treated, (c) OTS-coated APPJ-treated, (d) OTS-coated MEAs.

**Author Contributions:** Conceptualization, J.-Z.C.; methodology, all authors; validation, all authors; formal analysis, P.-Y.C.; investigation, P.-Y.C., N.-H.L., Y.-S.L.; writing—original draft preparation, P.-Y.C., J.-Z.C.; writing—review and editing, P.-Y.C., C.-H.C., Y.-L.L., J.-Z.C.; supervision, C.-H.C., Y.-L.L., J.-Z.C.; project administration, J.-Z.C.; funding acquisition, J.-Z.C., C.-H.C. All authors have read and agreed to the published version of the manuscript.

**Acknowledgments:** This study is financially supported by the “Advanced Research Center for Green Materials Science and Technology” from The Featured Area Research Center Program of the Higher Education Sprout Project by the Ministry of Education (108L9006) and the Ministry of Science and Technology in Taiwan (MOST 108-3017-F-002-002 and MOST 108-2221-E-002-088-MY3). CHC gratefully acknowledges funding support from the Young Scholar Fellowship Program of the Ministry of Science and Technology (MOST) in Taiwan (MOST 108-2636-E-002-006). We would like to thank Ms. Yuan-Tze Lee for her assistance with the SEM operation.

**Conflicts of Interest:** The authors declare no conflict of interest. The funders had no role in the design of the study; in the collection, analyses, or interpretation of data; in the writing of the manuscript, or in the decision to publish the results.

## References

1. Yeh, J.-W.; Chen, S.-K.; Lin, S.-J.; Gan, J.-Y.; Chin, T.-S.; Shun, T.-T.; Tsau, C.-H.; Chang, S.-Y. Nanostructured High-Entropy Alloys with Multiple Principal Elements: Novel Alloy Design Concepts and Outcomes. *Adv. Eng. Mater.* **2004**, *6*, 299–303. [[CrossRef](#)]
2. Kao, Y.-F.; Chen, T.-J.; Chen, S.-K.; Yeh, J.-W. Microstructure and mechanical property of as-cast, -homogenized, and -deformed  $\text{Al}_x\text{CoCrFeNi}$  ( $0 \leq x \leq 2$ ) high-entropy alloys. *J. Alloy. Compd.* **2009**, *488*, 57–64. [[CrossRef](#)]
3. Cantor, B.; Chang, I.; Knight, P.; Vincent, A. Microstructural development in equiatomic multicomponent alloys. *Mater. Sci. Eng. A* **2004**, *375*, 213–218. [[CrossRef](#)]
4. Luo, H.; Li, Z.; Mingers, A.M.; Raabe, D. Corrosion behavior of an equiatomic CoCrFeMnNi high-entropy alloy compared with 304 stainless steel in sulfuric acid solution. *Corros. Sci.* **2018**, *134*, 131–139. [[CrossRef](#)]
5. Rogachev, A.; Vadchenko, S.; Kochetov, N.; Rouvimov, S.; Kovalev, D.; Shchukin, A.; Moskovskikh, D.; Nepapushev, A.; Mukasyan, A. Structure and properties of equiatomic CoCrFeNiMn alloy fabricated by high-energy ball milling and spark plasma sintering. *J. Alloy. Compd.* **2019**, *805*, 1237–1245. [[CrossRef](#)]
6. Lu, T.; Chai, W.; Dai, T.; Pan, Y. FeCoNiCr<sub>0.5</sub>Al<sub>x</sub> High-Entropy Alloys with Dual-Phase Solidification Microstructure and High Compressive Properties. *JOM* **2019**, *71*, 3460–3465. [[CrossRef](#)]
7. Tong, Y.; Chen, D.; Han, B.; Wang, J.; Feng, R.; Yang, T.; Zhao, C.; Zhao, Y.; Guo, W.; Shimizu, Y.; et al. Outstanding tensile properties of a precipitation-strengthened FeCoNiCrTi<sub>0.2</sub> high-entropy alloy at room and cryogenic temperatures. *Acta Mater.* **2019**, *165*, 228–240. [[CrossRef](#)]
8. He, J.; Wang, H.; Wu, Y.; Liu, X.; Nieh, T.; Lu, Z. High-temperature plastic flow of a precipitation-hardened FeCoNiCr high entropy alloy. *Mater. Sci. Eng. A* **2017**, *686*, 34–40. [[CrossRef](#)]
9. Liu, W.; Yang, T.; Liu, C. Precipitation hardening in CoCrFeNi-based high entropy alloys. *Mater. Chem. Phys.* **2018**, *210*, 2–11. [[CrossRef](#)]
10. Veronesi, P.; Colombini, E.; Rosa, R.; Leonelli, C.; Garuti, M. Microwave processing of high entropy alloys: A powder metallurgy approach. *Chem. Eng. Process. Process. Intensif.* **2017**, *122*, 397–403. [[CrossRef](#)]
11. Wu, Z.; Bei, H.; Otto, F.; Pharr, G.; George, E. Recovery, recrystallization, grain growth and phase stability of a family of FCC-structured multi-component equiatomic solid solution alloys. *Intermetallics* **2014**, *46*, 131–140. [[CrossRef](#)]

12. Kai, W.; Li, C.C.; Cheng, F.P.; Chu, K.P.; Huang, R.T.; Tsay, L.W.; Kai, J.J. Air-oxidation of FeCoNiCr-based quinary high-entropy alloys at 700–900 °C. *Corros. Sci.* **2017**, *121*, 116–125. [[CrossRef](#)]
13. Qiu, X.-W.; Wu, M.-J.; Liu, C.-G.; Zhang, Y.-P.; Huang, C.-X. Corrosion performance of Al<sub>2</sub>CrFeCo<sub>x</sub>CuNiTi high-entropy alloy coatings in acid liquids. *J. Alloy. Compd.* **2017**, *708*, 353–357. [[CrossRef](#)]
14. Kumar, N.; Fusco, M.; Komarasamy, M.; Mishra, R.; Bourham, M.; Murty, K. Understanding effect of 3.5 wt.% NaCl on the corrosion of Al<sub>0.1</sub>CoCrFeNi high-entropy alloy. *J. Nucl. Mater.* **2017**, *495*, 154–163. [[CrossRef](#)]
15. Flater, E.; Ashurst, W.R.; Carpick, R.W. Nanotribology of Octadecyltrichlorosilane Monolayers and Silicon: Self-Mated versus Unmated Interfaces and Local Packing Density Effects. *Langmuir* **2007**, *23*, 9242–9252. [[CrossRef](#)]
16. Degen, P.; Shukla, A.; Boetcher, U.; Rehage, H. Self-assembled ultra-thin coatings of octadecyltrichlorosilane (OTS) formed at the surface of iron oxide nanoparticles. *Colloid Polym. Sci.* **2007**, *286*, 159–168. [[CrossRef](#)]
17. Chen, J.-Z.; Troian, S.M.; Darhuber, A.A.; Wagner, S. Effect of contact angle hysteresis on thermocapillary droplet actuation. *J. Appl. Phys.* **2005**, *97*, 14906. [[CrossRef](#)]
18. Wang, Y.; Lieberman, M. Growth of Ultrasoft Octadecyltrichlorosilane Self-Assembled Monolayers on SiO<sub>2</sub>. *Langmuir* **2003**, *19*, 1159–1167. [[CrossRef](#)]
19. Liu, Y.; Wolf, L.K.; Messmer, M.C. A study of alkyl chain conformational changes in self-assembled n-octadecyltrichlorosilane monolayers on fused silica surfaces. *Langmuir* **2001**, *17*, 4329–4335. [[CrossRef](#)]
20. Rozlosnik, N.; Gerstenberg, M.C.; Larsen, N.B. Effect of Solvents and Concentration on the Formation of a Self-Assembled Monolayer of Octadecylsiloxane on Silicon (001). *Langmuir* **2003**, *19*, 1182–1188. [[CrossRef](#)]
21. Akhtar, S.; Matin, A.; Kumar, A.M.; Ibrahim, A.; Laoui, T.; Ibrahim, A. Enhancement of anticorrosion property of 304 stainless steel using silane coatings. *Appl. Surf. Sci.* **2018**, *440*, 1286–1297. [[CrossRef](#)]
22. Vaidya, R.U.; Deshpande, A.; Hersman, L.; Brozik, S.M.; Butt, D. Protection of beryllium metal against microbial influenced corrosion using silane self-assembled monolayers. *Met. Mater. Trans. A* **1999**, *30*, 2129–2134. [[CrossRef](#)]
23. Winter, J.; Brandenburg, R.; Weltmann, K.-D. Atmospheric pressure plasma jets: An overview of devices and new directions. *Plasma Sources Sci. Technol.* **2015**, *24*, 64001. [[CrossRef](#)]
24. Brandenburg, R. Dielectric barrier discharges: Progress on plasma sources and on the understanding of regimes and single filaments. *Plasma Sources Sci. Technol.* **2017**, *26*, 053001. [[CrossRef](#)]
25. Brandenburg, R. Dielectric barrier discharges: Progress on plasma sources and on the understanding of regimes and single filaments (vol 26, 053001, 2017). *Plasma Sources Sci. Technol.* **2018**, *27*, 079501. [[CrossRef](#)]
26. Tendero, C.; Tixier, C.; Tristant, P.; Desmaison, J.; Leprince, P. Atmospheric pressure plasmas: A review. *Spectrochim. Acta Part B: At. Spectrosc.* **2006**, *61*, 2–30. [[CrossRef](#)]
27. Schütze, A.; Jeong, J.; Babayan, S.; Park, J.; Selwyn, G.; Hicks, R.F. The atmospheric-pressure plasma jet: A review and comparison to other plasma sources. *IEEE Trans. Plasma Sci.* **1998**, *26*, 1685–1694. [[CrossRef](#)]
28. Hsu, A.R.; Chien, H.-H.; Liao, C.-Y.; Lee, C.-C.; Tsai, J.-H.; Hsu, C.-C.; Cheng, I.-C.; Chen, J.-Z. Scan-Mode Atmospheric-Pressure Plasma Jet Processed Reduced Graphene Oxides for Quasi-Solid-State Gel-Electrolyte Supercapacitors. *Coatings* **2018**, *8*, 52. [[CrossRef](#)]
29. Takaki, K.; Hayashi, N.; Wang, D.; Ohshima, T. High-voltage technologies for agriculture and food processing. *J. Phys. D Appl. Phys.* **2019**, *52*, 473001. [[CrossRef](#)]
30. Šimončicová, J.; Kryštofová, S.; Medvecká, V.; Ďurišová, K.; Kalinaková, B. Technical applications of plasma treatments: Current state and perspectives. *Appl. Microbiol. Biotechnol.* **2019**, *103*, 5117–5129. [[CrossRef](#)]
31. Kuok, F.-H.; Liao, C.-Y.; Wan, T.-H.; Yeh, P.-W.; Cheng, I.-C.; Chen, J.-Z. Atmospheric pressure plasma jet processed reduced graphene oxides for supercapacitor application. *J. Alloy. Compd.* **2017**, *692*, 558–562. [[CrossRef](#)]
32. Xu, C.H.; Shen, P.Y.; Chiu, Y.F.; Yeh, P.W.; Chen, C.C.; Chen, L.C.; Hsu, C.C.; Cheng, I.C.; Chen, J.Z. Atmospheric pressure plasma jet processed nanoporous Fe<sub>2</sub>O<sub>3</sub>/CNT composites for supercapacitor application. *J. Alloy. Compd.* **2016**, *676*, 469–473. [[CrossRef](#)]
33. Wu, T.-H.; Cheng, I.-C.; Hsu, C.-C.; Chen, J.-Z.; Hsu, C.-C. UV photocurrent responses of ZnO and MgZnO/ZnO processed by atmospheric pressure plasma jets. *J. Alloy. Compd.* **2015**, *628*, 68–74. [[CrossRef](#)]
34. Wu, C.H.; Chen, J.Z. Ultrafast atmospheric-pressure-plasma-jet processed conductive plasma-resistant Y<sub>2</sub>O<sub>3</sub>/carbon-nanotube nanocomposite. *J. Alloy. Compd.* **2015**, *651*, 357–362. [[CrossRef](#)]

35. Chen, J.-Z.; Hsu, C.-C.; Wang, C.; Liao, W.-Y.; Wu, C.-H.; Wu, T.-J.; Liu, H.-W.; Chang, H.; Lien, S.-T.; Li, H.-C.; et al. Rapid Atmospheric-Pressure-Plasma-Jet Processed Porous Materials for Energy Harvesting and Storage Devices. *Coatings* **2015**, *5*, 26–38. [[CrossRef](#)]
36. Wan, T.-H.; Chiu, Y.-F.; Chen, C.-W.; Hsu, C.-C.; Cheng, I.-C.; Chen, J.-Z. Atmospheric-Pressure Plasma Jet Processed Pt-Decorated Reduced Graphene Oxides for Counter-Electrodes of Dye-Sensitized Solar Cells. *Coatings* **2016**, *6*, 44. [[CrossRef](#)]
37. Chien, H.-H.; Liao, C.-Y.; Hao, Y.-C.; Hsu, C.-C.; Cheng, I.-C.; Yu, I.-S.; Chen, J.-Z. Improved performance of polyaniline/reduced-graphene-oxide supercapacitor using atmospheric-pressure-plasma-jet surface treatment of carbon cloth. *Electrochim. Acta* **2018**, *260*, 391–399. [[CrossRef](#)]
38. Chang, H.; Yang, Y.-J.; Li, H.-C.; Hsu, C.-C.; Cheng, I.-C.; Chen, J.-Z.; Hsu, C.-C. Preparation of nanoporous TiO<sub>2</sub> films for DSSC application by a rapid atmospheric pressure plasma jet sintering process. *J. Power Sources* **2013**, *234*, 16–22. [[CrossRef](#)]
39. Chang, H.; Hsu, C.-M.; Kao, P.-K.; Yang, Y.-J.; Hsu, C.-C.; Cheng, I.-C.; Chen, J.-Z.; Hsu, C.-C. Dye-sensitized solar cells with nanoporous TiO<sub>2</sub> photoanodes sintered by N<sub>2</sub> and air atmospheric pressure plasma jets with/without air-quenching. *J. Power Sources* **2014**, *251*, 215–221. [[CrossRef](#)]
40. Liao, W.-Y.; Yang, Y.-J.; Hsu, C.-M.; Hsu, C.-C.; Cheng, I.-C.; Chen, J.-Z.; Hsu, C.-C. Atmospheric-pressure-plasma-jet sintered dual-scale porous TiO<sub>2</sub> using an economically favorable NaCl solution. *J. Power Sources* **2015**, *281*, 252–257. [[CrossRef](#)]
41. Chang, S.-H.; Liou, J.-S.; Liu, J.-L.; Chiu, Y.-F.; Xu, C.-H.; Chen, B.-Y.; Chen, J.-Z. Feasibility study of surface-modified carbon cloth electrodes using atmospheric pressure plasma jets for microbial fuel cells. *J. Power Sources* **2016**, *336*, 99–106. [[CrossRef](#)]
42. Saleema, N.; Gallant, D. Atmospheric pressure plasma oxidation of AA6061-T6 aluminum alloy surface for strong and durable adhesive bonding applications. *Appl. Surf. Sci.* **2013**, *282*, 98–104. [[CrossRef](#)]
43. Regula, C.; Ihde, J.; Lommatzsch, U.; Wilken, R. Corrosion protection of copper surfaces by an atmospheric pressure plasma jet treatment. *Surf. Coat. Technol.* **2011**, *205*, S355–S358. [[CrossRef](#)]
44. Li, P.; Li, L.; Wang, W.; Jin, W.; Liu, X.; Yeung, K.; Chu, P.K. Enhanced corrosion resistance and hemocompatibility of biomedical NiTi alloy by atmospheric-pressure plasma polymerized fluorine-rich coating. *Appl. Surf. Sci.* **2014**, *297*, 109–115. [[CrossRef](#)]
45. Aghuy, A.A.; Zakeri, M.; Moayed, M.; Mazinani, M. Effect of grain size on pitting corrosion of 304L austenitic stainless steel. *Corros. Sci.* **2015**, *94*, 368–376. [[CrossRef](#)]
46. Vyas, A.; Shen, Y.; Zhou, Z.; Li, K.Y. Nano-structured CrN/CN<sub>x</sub> multilayer films deposited by magnetron sputtering. *Compos. Sci. Technol.* **2008**, *68*, 2922–2929. [[CrossRef](#)]
47. De La Cruz, W.; Contreras, O.; Soto, G.; Pérez-Tijerina, E. Cobalt nitride films produced by reactive pulsed laser deposition. *Rev. Mex. Fis.* **2006**, *52*, 409–412.
48. Tan, B.J.; Klabunde, K.J.; Sherwood, P.M.A. XPS studies of solvated metal atom dispersed (SMAD) catalysts. Evidence for layered cobalt-manganese particles on alumina and silica. *J. Am. Chem. Soc.* **1991**, *113*, 855–861. [[CrossRef](#)]
49. Davidson, A.; Tempere, J.F.; Che, M.; Roulet, H.; Dufour, G. Spectroscopic Studies of Nickel(II) and Nickel(III) Species Generated upon Thermal Treatments of Nickel/Ceria-Supported Materials. *J. Phys. Chem.* **1996**, *100*, 4919–4929. [[CrossRef](#)]
50. Nishimura, O.; Yabe, K.; Iwaki, M. X-ray photoelectron spectroscopy studies of high-dose nitrogen ion implanted-chromium: A possibility of a standard material for chemical state analysis. *J. Electron Spectrosc. Relat. Phenom.* **1989**, *49*, 335–342. [[CrossRef](#)]
51. Biesinger, M.C.; Brown, C.; Mycroft, J.R.; Davidson, R.D.; McIntyre, N.S. X-ray photoelectron spectroscopy studies of chromium compounds. *Surf. Interface Anal.* **2004**, *36*, 1550–1563. [[CrossRef](#)]

